Rare Metal Materials and Engineering
Volume 55, Issue 6, June 2026
Available online at www.rmme.ac.cn

Science Press

Cite this article as: Li Congwei, Zhu Jialei, Zeng Caiyou, et al. Enhanced Wear Resistance of ULDLC Duplex Stainless Steel Coating via Laser Remelting[J]. Rare Metal Materials and Engineering, 2026, 55(06): 1385-1392. DOI: https://doi.org/10.12442/j.issn.1002-185X.20250266.

ARTICLE

Enhanced Wear Resistance of ULDLC Duplex Stainless Steel Coating via Laser Remelting

Li Congwei[1,2], Zhu Jialei[2], Zeng Caiyou[2], Deng Caiyan[1], Cong Baoqiang[3], Cui Lei[1], Jiao Xiangdong[2]

[1] School of Materials Science and Engineering, Tianjin University, Tianjin 300354, China; [2] School of Mechanical Engineering, Beijing Institute of Petrochemical Technology, Beijing 102617, China; [3] School of Mechanical Engineering and Automation, Beihang University, Beijing 102206, China

Abstract: Underwater local dry laser cladding (ULDLC) is a key technique for in-situ repair of nuclear power equipment. In this study, an underwater laser remelting technique was proposed to further enhance the wear resistance of duplex stainless steel (DSS) coatings prepared by ULDLC. The effects of laser remelting heat input on the microstructure and wear resistance of DSS coating prepared by ULDLC were investigated. Results indicate that the microstructure of DSS coatings consists of Widmanstätten austenite (WA), intergranular austenite (IGA), grain boundary austenite, secondary austenite (γ_2), and ferrite. With the increase in laser remelting heat input, the content of IGA and WA gradually decreases, while the ferrite content increases. After laser remelting, γ_2 is eliminated and the grain morphology of ferrite is transformed from flaky to equiaxed. Under optimal laser remelting parameters (a laser power of 3 kW, a laser spot diameter of 6 mm, and a laser scanning speed of 10 mm/s), the microhardness of remelted zone is 318.7 HV, which is increased by 25.7 HV, the friction coefficient decreases by 32%, and the wear volume is reduced by 55%. The significantly improved wear resistance is attributed to the synergistic effects of surface oxide-layer formation and ferrite grain refinement.

Key words: nuclear power equipment; underwater laser cladding; laser remelting; duplex stainless steel; wear resistance

1 Introduction

Duplex stainless steels (DSSs) exhibit superior corrosion resistance and mechanical properties, which is attributed to their dual-phase microstructure (ferrite α+austenite γ)[1–3] and high content of alloying element[4]. In recent decades, DSS has found widespread applications in oil/gas industries, flue gas purification systems, and nuclear power plants (NPPs)[5]. DSS is also a viable alternative to austenitic stainless steel, super austenitic steel[6–7], and certain nickel-based alloys[8–10]. As early-generation NPPs approach their design lifetimes, lifetime extension strategies have garnered significant attention. This is primarily attributed to the need for prolonging service life of irreplaceable components[11], such as reactor vessel interior positioning key/keyway, spent fuel pool, refueling pool, and seawater condensation system pipeline, which are generally made of DSS[12–13].

During NPP material changes and maintenance processes, the wear of the radial support key/keyway of the hoist basket cylinder is inevitable, which leads to wear failure. Wear is caused by steel cladding on the bottom surface of the spent fuel pool during transportation of spent fuel assemblies. The high flow velocity of some part of seawater system in NPPs accelerates damages of components[14]. Tribological wear synergistically accelerates corrosion[15], thereby compromising operational safety of NPPs. Consequently, investigating underwater emergency repair techniques for DSS, along with their

Received date: June 15, 2025
Foundation item: National Natural Science Foundation of China (U22B20127, 52305331); Beijing Municipal Science and Technology Project (KZ202210017023); Beijing Municipal HEI Research Innovation Team Program (BPHR20220110); Hebei Provincial Key Research and Development Program Project (22341801D, 23311802D)
Corresponding author: Zhu Jialei, Ph. D., Professor, School of Mechanical Engineering, Beijing Institute of Petrochemical Technology, Beijing 102617, P. R. China, Tel: 0086-10-81292134, E-mail: zhujialei@bipt.edu.cn;Zeng Caiyou, Ph. D., Associate Professor, School of Mechanical Engineering, Beijing Institute of Petrochemical Technology, Beijing 102617, P. R. China, E-mail: zengcy@bipt.edu.cn

associated microstructural evolution mechanisms and mechanical property changes, becomes imperative.

Underwater cladding technique enables in-situ repair of damaged components. Laser cladding demonstrates exceptional suitability for underwater applications due to its precise heat control and superior process stability. Two principal underwater laser cladding techniques exist, including wet laser cladding and underwater local dry laser cladding (ULDLC). Although wet laser cladding requires simple equipment, the presence of water adversely affects the laser transmission and weld quality[16–18]. ULDLC creates a protective gas environment that shields the melt pool and prevents water interference with beam transmission through drainage units[19–21]. Related studies confirm the technical superiority and greater developmental potential of ULDLC over wet laser cladding.

Laser remelting enables in-situ coating reheating[22], inducing rapid melting-solidification cycles that modify microstructure and surface morphology, and consequently enhances surface properties. Hwang et al[23] investigated how key process parameters (scanning number, beam scanning pattern, and hatch spacing) influence surface roughness and hardness in underwater wet laser remelting. Previous studies[24] attribute the enhanced microhardness to synergistic effects of grain-refinement strengthening and solid-solution strengthening mechanisms. Cai et al[25] demonstrated that multi-pass in-situ laser remelting effectively eliminates stress concentration zones and significantly improves wear resistance of coating. Through comparative analysis of laser cladding and remelting processes, Cai et al[26] achieved a remarkable microhardness enhancement (900 HV) in Ni-Cr-Co-Ti-V high-entropy alloy coatings. Chen et al[27] confirmed superior and more homogeneous hardness distribution on the surfaces compared to the substrate of laser-remelted A384.

Nevertheless, the synergistic application of laser cladding and remelting techniques for DSS coating preparation in underwater environments remains underexplored. S32101 DSS coatings could be prepared using ULDLC at water depth of 500 mm, integrating both cladding and remelting processes. Systematic investigations were conducted on how varying laser-remelting linear-energy affects the morphology, microstructure evolution, microhardness distribution, and wear resistance of ULDLC-prepared coatings. The study elucidated the microstructure evolution mechanisms and performance enhancement of DSS coatings under simulated underwater emergency maintenance conditions.

2 Experiment

S32101 DSS (300 mm×150 mm×16 mm) was used as substrate, and the filler metal was welding wire (grade ER2209) with a diameter of 1.2 mm. Chemical composition of above materials is listed in Table 1.

The experimental setup for ULDLC and laser remelting comprised a custom-designed underwater laser processing system (Fig. 1a), including an RCL-6000 laser source, a specialized underwater cladding head, a waterproof three-axis translational stage immersed in a water tank, and a centralized control system. The substrate was immersed at water depth of 500 mm with maintained ambient temperature of 22±0.5 °C. A locally mounted drainage assembly was precisely aligned with the substrate surface. High-purity argon (99.99%) was continuously supplied through internal channels to establish a dry zone, effectively shielding the molten pool from water intrusion (Fig. 1b). Real-time molten pool monitoring was achieved via a coaxial CCD imaging system integrated within the cladding head (Fig.1c).

Table 1 Chemical composition of substrate and filler metal (wt%)

Material	C	Mo	Mn	Ni	Cr	Fe
S32101 DSS	0.023	0.26	4.90	1.62	21.50	Bal.
ER2209 filler metal	0.012	3.05	1.59	8.62	22.56	Bal.

Prior to processing, the substrate was mechanically polished using a stainless steel wire brush, followed by sequential degreasing with anhydrous ethanol and acetone in an ultrasonic bath. The base material (BM) was positioned at 500 mm in water depth. ULDLC was performed in two parallel passes (48% overlap rate) along identical trajectories (Fig.2a). Optimal cladding parameters were determined through systematic parameter optimization: laser power of 5 kW, beam diameter of 5 mm, scanning velocity of 10 mm/s, shielding gas flow rate of 50 L/min, and wire feed rate of 420 cm/min. Following dual-channel cladding, the coatings underwent two-passes laser remelting along the original deposition paths. Detailed remelting parameters are summarized in Table 2. Specimens were designated as W1, W2, W3, and W4 corresponding to applied linear energy densities of 0, 100, 300, and 500 J/mm, respectively. Fig. 2b illustrates the standardized sampling methodology for subsequent characterization.

The metallographic specimens were sectioned perpendicular to the coating surface using electrical discharge

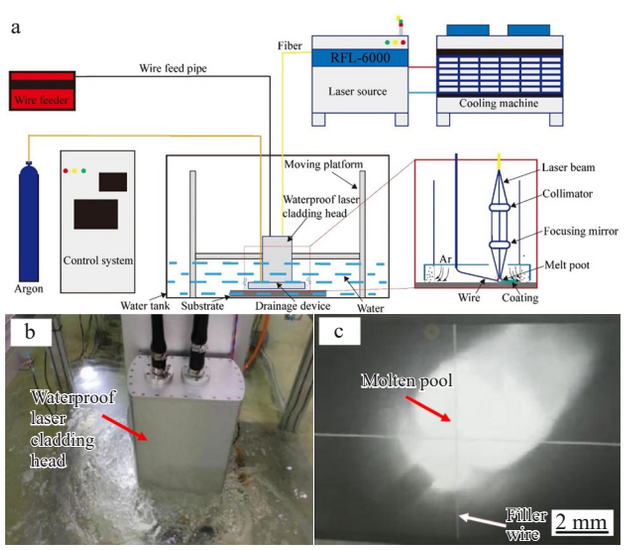

Fig.1 Schematic diagram of the underwater cladding system (a); appearance of underwater cladding experimental process (b); real-time monitoring image of molten pool (c)

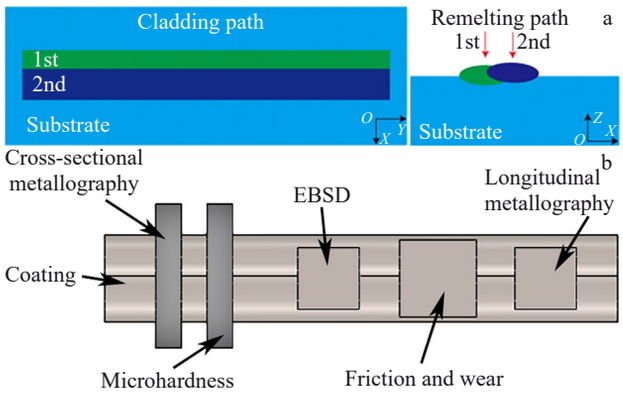

Fig.2 Schematic diagrams of the cladding path (a) and sampling positions (b)

machine, then mounted in epoxy resin, and sequentially ground with SiC abrasive paper (180#–2000#) under ambient conditions. Following mechanical polishing, the specimens were chemically etched using a $FeCl_3$-HCl aqueous solution (10vol%). Microstructural characterization was performed using optical microscope (OM), while phase distribution, crystallographic orientation, and grain size analysis were conducted via electron backscatter diffractometer (EBSD). Vickers microhardness measurements were performed using an HVS-1000Z tester with a load of 4.9 N and dwell time of 10 s.

Reciprocating sliding wear tests were conducted using a Bruker UMT TriboLab tribometer under controlled ambient conditions (22±1 °C, relative humidity of 40%–60%). Test parameters included the normal load of 15 N, the WC-Co counterbody diameter of 6 mm, the stroke length of 3 mm, and the oscillation frequency of 10 Hz. Post-test analysis involved 3D profilometer (Bruker ContourX-100) for quantitative wear scar characterization, including surface roughness evaluation. Wear mechanisms were identified through scanning electron microscope (SEM, Hitachi TM4000-II).

3 Results and Discussion

3.1 Appearance and characteristics

Fig.3 compares the surface morphologies of specimens W1 and W4, revealing topographical differences resulting from varying laser remelting energy densities. As shown in Fig.3a, specimen W1 exhibits pronounced surface roughness, which is attributed to constrained molten pool flow caused by rapid solidification during ULDLC, leading to non-equilibrium solidification with incomplete liquid metal spreading. Laser remelting induces coating remelting, where thermal expansion and surface tension effects (including capillary and Marangoni forces) facilitate complete molten pool redistribution[27–28]. Consequently, surface irregularities are effectively eliminated through this homogenization process. Therefore, specimen W4 demonstrates superior surface quality, characterized by enhanced metallic luster and significantly reduced surface roughness (Fig.3b).

3.2 Microstructure

Fig.4–Fig.7 present the microstructural evolution of specimens W1–W4, demonstrating distinct phase distributions in different processing zones. Distinct coating-substrate interfaces with well-defined fusion lines confirm optimal metallurgical bonding (Fig. 4) [29]. The remelting zone (RZ) depth exhibits a linear dependence on applied linear energy density, as demarcated by the red dashed line in Fig.4 (RZ is above the line). RZ depths of specimens W2, W3, and W4 are 0.425, 1.537, and 2.655 mm, respectively.

Fig. 5 shows the cross-sectional microstructures of specimens. The W1 coating (Fig.5a) reveals near-equilibrium dual-phase structures (δ-ferrite+γ-austenite), containing grain boundary austenite (GBA), intragranular austenite (IGA), and Widmanstätten austenite (WA), along with secondary γ_2 phases. This phase constitution agrees with previous report[30], whereas δ-phase precipitates are not observed in this study.

Fig. 5b – 5d present the microstructural characteristics of laser-remelted coatings W2–W4, revealing significant phase fraction variations with the increase in linear energy density. Laser remelting promotes δ-ferrite grain clustering while suppressing γ-austenite formation, which is primarily attributed to the combined effects of rapid scanning speed (10 mm/s) [31] and water-quenching (500 mm in depth) [21], increasing the cooling rate beyond 10^3 K/s. The $\delta \rightarrow \gamma$ phase transformation, normally occurring within the range of 800–1200 °C, is inhibited by reduced thermal residence time (<0.5 s) in this critical temperature range.

Fig. 6 demonstrates consistent microstructural evolution trends between wear test zones and coating cross-sections, confirming homogeneous phase distribution. Progressive heat input elevation from 100 J/mm to 500 J/mm leads to a reduction in IGA, disappearance of WA, and the increase in δ-ferrite content. Meanwhile, the γ_2 phase is completely dissolved, and δ-ferrite grain morphology is transformed from lamellar to equiaxed.

Phase analysis of specimens W1 and W3 was conducted via X-ray diffraction (XRD), and the result reveals that laser remelting reduces the peak intensities of γ-austenite diffraction planes (111), (200), (220), and (311) in DSS coating, as shown in Fig. 7. Concurrently, the intensity of the δ-ferrite

Table 2 Process parameters of ULDLR

Specimen	Remelting speed/mm·s^{-1}	Focal spot diameter/mm	Laser power/kW	Shielding gas flow/L·min^{-1}	Linear energy density/J·mm^{-1}
W1	-	-	-	-	0
W2	10	6	1	50	100
W3	10	6	3	50	300
W4	10	6	5	50	500

Fig.3 Coating appearances and characteristics of specimens W1 (a) and W4 (b)

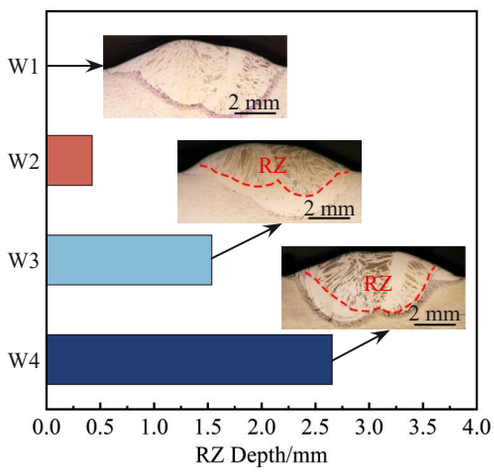

Fig.4 Comparison of RZ depths of specimens W1−W4

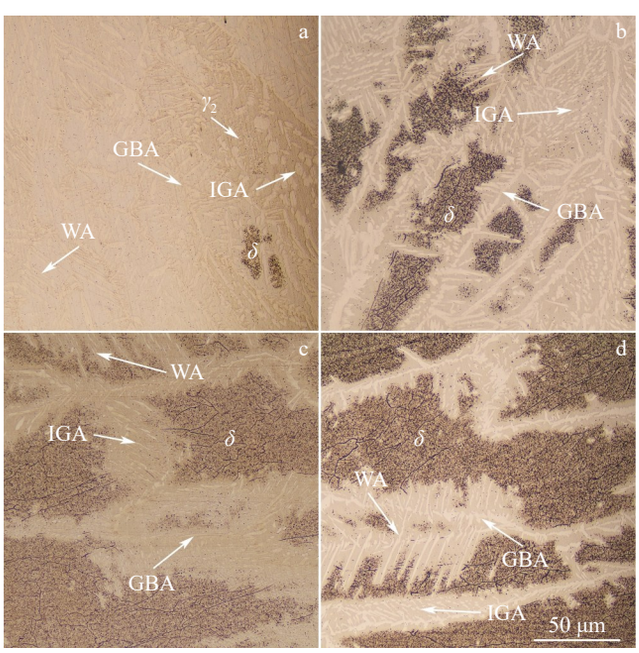

Fig.5 Microstructures of cross-sections of specimens: (a) W1, (b) W2, (c) W3, and (d) W4

(211) plane decreases, while that of the δ-ferrite (110) plane increases. No characteristic diffraction peaks of intermetallic compounds are detected in XRD patterns, as their contents are below the detection limit (<2wt%).

To quantitatively analyze the phase distribution, grain morphology, boundary misorientation, and crystallographic texture, the longitudinal section of specimen W3 was

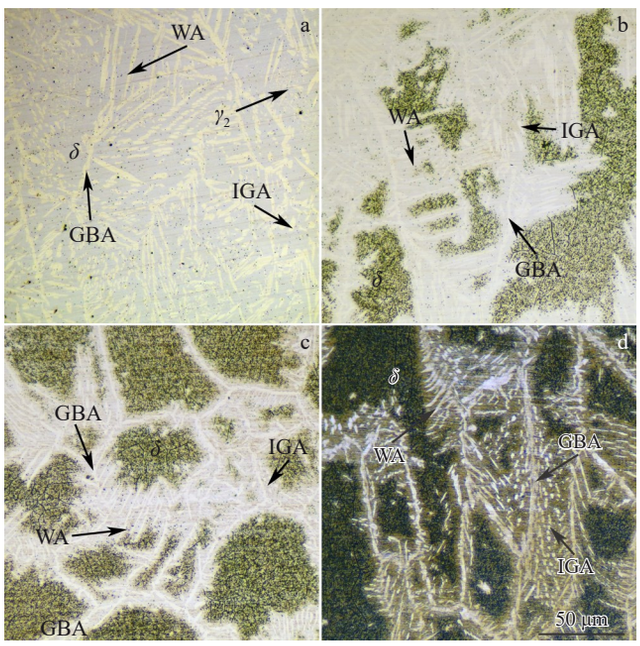

Fig.6 Microstructures of longitudinal sections of specimens: (a)W1, (b)W2, (c) W3, and (d) W4

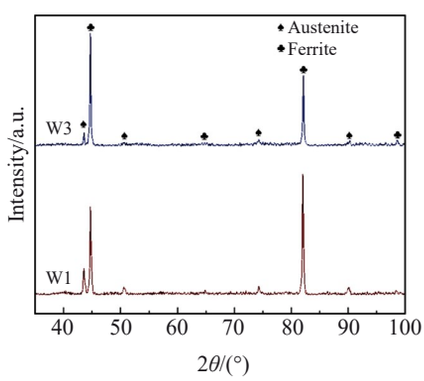

Fig.7 XRD patterns of specimens W1 and W3

characterized by EBSD (Fig.8–Fig.9). The inverse pole figure (IPF) demonstrates random δ -ferrite grain orientations (Fig. 8a), while γ -austenite exhibits morphological diversity dominated by GBA and IGA variants. Quantitative phase analysis reveals a dramatic γ:δ ratio shift (0.09:98.1) for the laser-remelted specimen compared to air-processed DSS (Fig. 8b), which is attributed to cumulative thermal effects from multi-pass remelting with rapid water cooling.

Grain boundaries (GBs) delineate crystallographic orientation mismatches between adjacent grains. According to misorientation angle (θ), GBs are classified as: low-angle GBs (LAGBs, $\theta<5°$), medium-angle GBs (MAGBs, $5°\leqslant\theta\leqslant15°$), and high-angle GBs (HAGBs, $\theta>15°$). Fig. 8c – 8d present the misorientation angle distributions for δ-ferrite/γ-austenite interfaces in specimen W3, γ-austenite exhibits bimodal misorientation distribution (peaks at 2° and 60°), reflecting that epitaxial growth is constrainted during rapid solidification. δ-ferrite contains 40% LAGBs and 52% HAGBs, with maximum frequency at 2° misorientation.

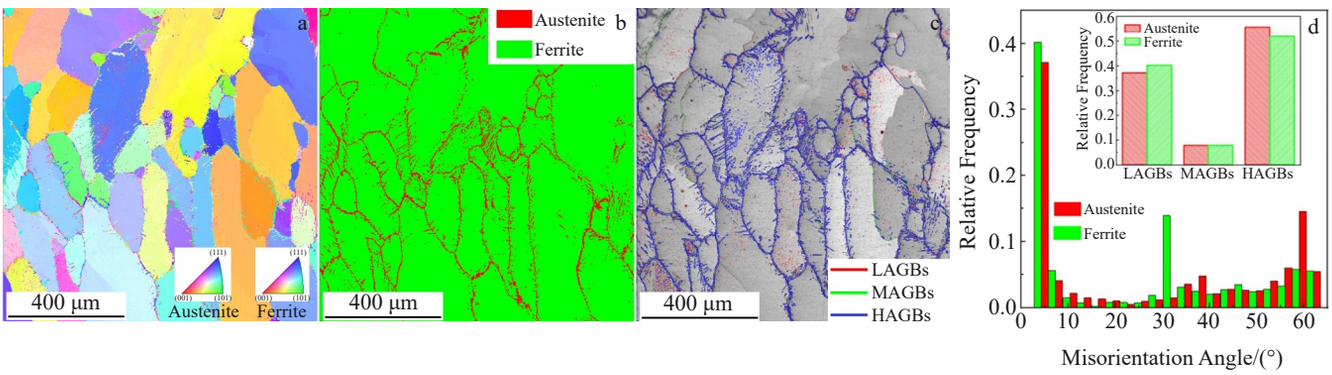

Fig.8 EBSD analysis of specimen W3: (a) IPF, (b) phase map, (c) GB map, and (d) misorientation distributions of ferrite and austenite

Crystallographic texture analysis via pole figure (PF) reveals distinct orientation preferences (Fig. 9). δ -ferrite exhibits R-cube texture {001}<100>, whereas γ-austenite is characterized by strong Goss texture {110}<100>.

3.3 Microhardness

Fig. 10 presents the microhardness variation across the BM-coating interface, measured perpendicular to the fusion line. Given the comparable composition of filler wire and substrate (Table 1), microhardness variations primarily reflect ULDLC processing effects. The substrate exhibits an average microhardness of 284.0 HV, while laser-remelted zones (LRZ) of specimens W2, W3, and W4 exhibit increased microhardness values of 297.9, 309.7, and 309.7 HV, respectively. The average microhardness of W1 specimen is 299.3 HV. Previous studies[22,31] confirm that the precipitation of Cr_2N in DSS intensifies with cooling rate exceeding 100 K/s. Extensive Cr_2N precipitation (Fig. 10) contributes significantly to coating hardening[32–33]. Peak microhardness (318.7 HV) in specimen W3 is located within Cr_2N-rich regions. Compared with specimen W1, the reduced micro-hardness in LRZ of specimen W2 suggests that Cr_2N precipitation hardening dominates over the grain-refinement strengthening effect associated with γ-austenite. Elevated laser power in specimen W4 enhances melt penetration, increasing microhardness of heat affected zone (HAZ) through promoting Cr_2N precipitation. Compared with specimen W3, lower average microhardness of specimen W4 reflects reduced cooling rates due to higher power input, decreasing Cr_2N nucleation density.

3.4 Wear behavior

Fig. 11 shows the coefficient of friction (COF) curves obtained from wear tests of specimens W1–W4 under a load of 15 N. At the beginning of the test, the coating surface is damaged, the surface roughness of the coating increases, and COF rises rapidly. As the test continues, the contact area between the grinding ball and coating increases, and the load is carried by a large area, thus decreasing the pressure. This promotes the transition to steady-state wear with stabilized COF. The heterogeneous Cr_2N distribution leads to localized microhardness variations (290–320 HV) across wear tracks[34]. COF of specimen W1 maintains pronounced fluctuations (standard deviation, σ =0.15) during steady-state stage. And specimens W2, W3, and W4 exhibit steady-state COF values of 1.20±0.05, 1.15±0.03, and 1.25±0.07, respectively. Speci-

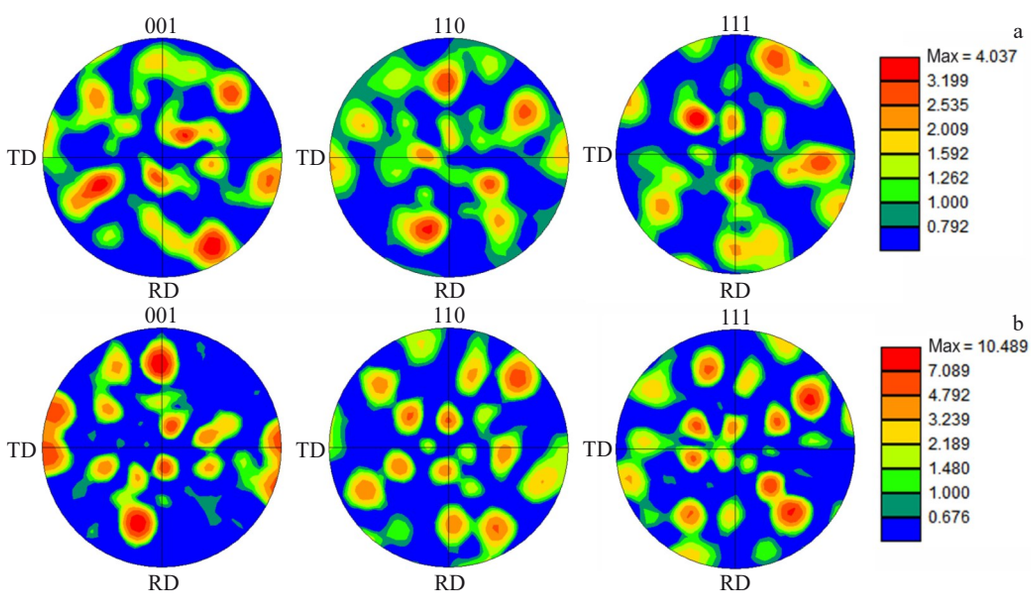

Fig.9 PFs of specimen W3: (a) austenite; (b) ferrite (TD indicates transverse direction; RD indicates rolling direction)

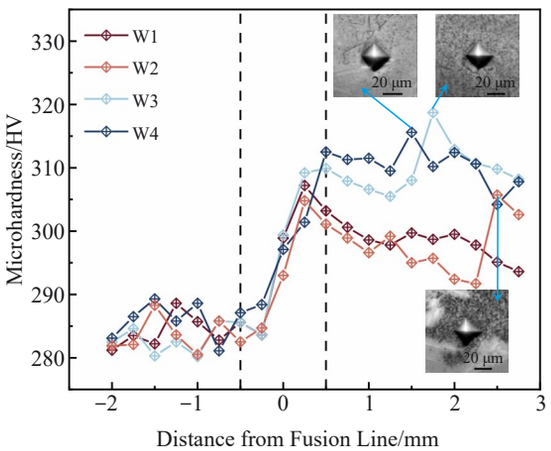

Fig.10 Microhardness variation across BM-coating interface

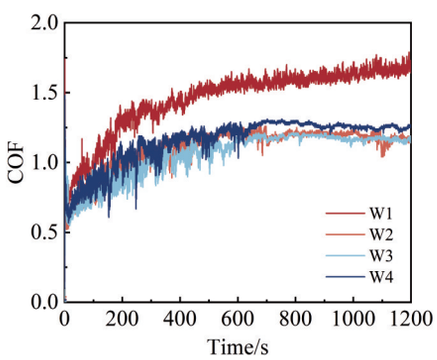

Fig.11 COF curves obtained from wear tests of specimens W1–W4 under a load of 15 N

men W3 reaches steady state the earliest (at 600 s) and demonstrates the most stable friction behavior (σ=0.02). And COF value of specimen W3 is reduced by 32% compared with that of specimen W1.

Fig. 12 presents wear morphologies across specimens W1–W4, revealing distinct surface damage features. The edges of wear tracks exhibit significant topographical variations, which is attributed to pronounced plastic deformation and parallel grooving. Severe plastic flow causes the material to move laterally along the grinding groove, forming characteristic piled-up ridges. The relatively lower microhardness of specimen W1 (299.3 HV) results in 40% greater deformation depth compared to other specimens. The parallel grooves originate from micro-cutting and plowing mechanisms, consistent with classical two-body abrasive wear behavior[35]. Groove centers exhibit oxidative wear features and delamination cracks, where cyclic loading induces subsurface fatigue cracking and subsequent material spallation[36].

To quantitatively evaluate wear scar topography, Fig. 13 summarizes the height parameters of the abrasion mark and surrounding area, together with volume loss. In Fig. 13a, MH means maximum height, MSH represents mean summit height, and AMH means arithmetic mean height. Specimen W1 shows the highest value of MH/MSH/AMH, indicating a deeper groove and more severe relief from plastic deformation and damage, whereas specimen W3 has the lowest values, suggesting a shallower, smoother scar. Specimens W2 and W4 are intermediate. Volume loss in Fig. 13b directly reflects material removal and follows the same trend. Notably, specimen W3 loses only 0.056 mm^3 in volume, which exhibits a 55% decrease compared to specimen W1, confirming its superior wear resistance.

SEM was employed to examine the abrasion marks in detail and study their wear mechanisms. Fig. 14 reveals plow grooves accompanied by substantial plastic deformation in the coatings, which are characteristics of abrasive wear mechanisms[35]. Plastic-deformed abrasive debris accumulates along the wear scar periphery. Specimen W1 exhibits more

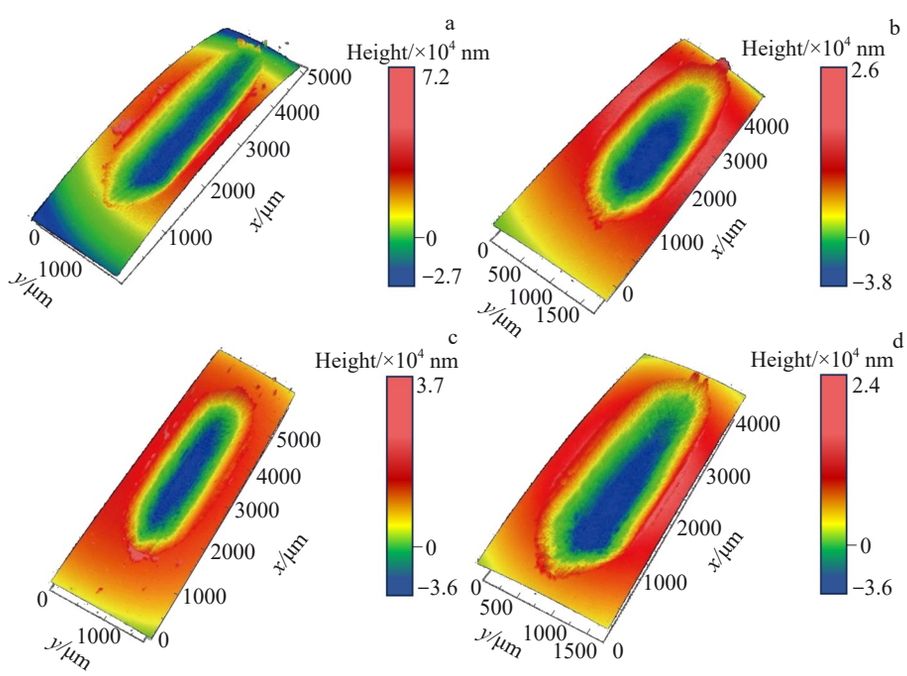

Fig.12 Three-dimensional profiles of the worn surface appearances: (a) W1, (b) W2, (c) W3, and (d) W4

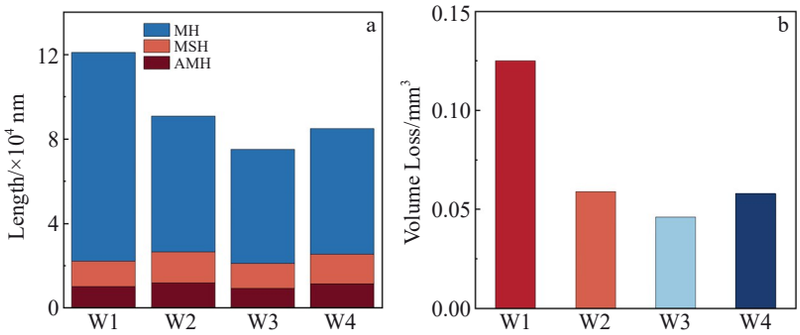

Fig.13 Height parameters (a) and volume loss (b) of abrasion mark and the surrounding area of different specimens

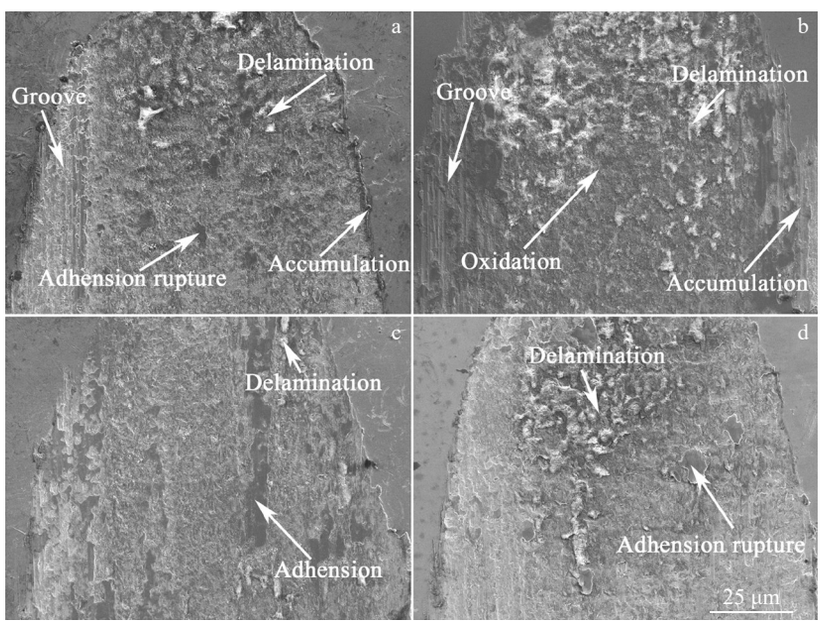

Fig.14 SEM images of the abrasion marks of different specimens: (a) W1; (b) W2; (c) W3; (d) W4 of different specimens

pronounced debris accumulation near the wear scar. Fig. 14 additionally demonstrates surface delamination and oxidation phenomena. The delamination is due to fatigue wear with various degrees as the surface undergoes repeated loading during the wear process[36]. Partial abrasive debris adheres to the wear surface, through which the grinding ball transmits external loads. During ball movement, these adhered particles slide, exhibiting adhesive wear behavior[37]. Adhered abrasive chips under reciprocating loads produce adhesion ruptures.

4 Conclusions

1) The combined effects of thermal expansion and surface tension promote complete molten pool redistribution, significantly enhancing coating surface quality. The as-deposited W1 coating exhibits near-equilibrium dual-phase microstructure (δ-ferrite+γ-austenite), including GBA, IGA, WA, γ_2, and ferrite.

2) With the increase in linear energy density during laser remelting, the microstructure evolution exhibits a reduction in IGA, the disappearance of WA, an increase in δ content, complete dissolution of γ_2 phase, and grain morphology transition of δ-ferrite from lamellar to equiaxed. This microstructural evolution results in a 25.7 HV increase in microhardness, with peak microhardness of 318.7 HV observed in Cr_2N-rich zones.

3) Laser remelting achieves optimal tribological performance at 300 J/mm by refining δ grains and enhancing atomic bonding. The friction coefficient deceases to 1.15 (a 32% reduction), while wear volume is 0.056 mm^3 (a 55% decrease), which is attributed to combined effects of grain refinement and Cr_2N precipitation hardening.

References

1 Lo K H, She C H, Lai J K L. *Materials Science and Engineering R: Reports*[J], 2009, 65(4–6): 39

2 Davison R M, Redmond J D. *Materials & Design*[J], 1991, 12(4): 187

3 da Cruz Junior E J, Franzini O D, Calliari I *et al*. *Metallurgical and Materials Transactions A*[J], 2019, 50(4): 1616

4 Zhang W, Jiang L Z, Gao J Q *et al*. *Materials Science and Technology*[J], 2010, 26(5): 515

5 Zhang W, Jiang L Z, Hu J C *et al*. *Materials Science and*

Engineering A[J], 2008, 497(1–2): 501
6 Boillot P, Peultier J. *Procedia Engineering*[J], 2014, 83: 309
7 Hu Y, Shi Y H, Sun K *et al*. *Journal of Materials Processing Technology*[J], 2018, 261: 31
8 Francis R, Byrne G. *Metals*[J], 2021, 11(5): 836
9 Nomani J, Pramanik A, Hilditch T *et al*. *Wear*[J], 2013, 304(1–2): 20
10 Koyee R D, Heisel U, Eisseler R *et al*. *Journal of Manufacturing Processes*[J], 2014, 16(4): 451
11 Ti W X, Wu H C, Xue F *et al*. *Nuclear Engineering and Technology*[J], 2021, 53(8): 2591
12 Fan Y, Liu T G, Xin L *et al*. *Journal of Nuclear Materials*[J], 2021, 544: 152693
13 Ahn S K, Jang Y Y. *Corrosion Science and Technology*[J], 2011, 10(2): 60
14 Chang H Y, Park H B, Park Y S *et al*. *Corrosion Science and Technology*[J], 2010, 9(5): 187
15 Mischler S, Debaud S, Landolt D. *Journal of the Electrochemical Society*[J], 1998, 145(3): 750
16 You Jiayu, Hu Chenyu, Zhang Zhenhai *et al*. *Rare Metal Materials and Engineering*[J], 2024, 53(8): 2314 (in Chinese)
17 Cai Z H, Du X, Zhu J L *et al*. *Materials*[J], 2022, 15(9): 3380
18 Wen X, Jin G, Cui X F *et al*. *Optics & Laser Technology*[J], 2019, 111: 814
19 Guo N, Fu Y L, Xing X *et al*. *Journal of Materials Processing Technology*[J], 2018, 260: 146
20 Luo M L, Wei P Y, Li Q H *et al*. *Metals*[J], 2021, 11(4): 610
21 Fu Y L, Guo N, Cheng Q *et al*. *Journal of Materials Research and Technology*[J], 2020, 9(6): 15648
22 Zhu Jing, Hua Yuting, He Qingsheng *et al*. *Rare Metal Materials and Engineering*[J], 2023, 52(5): 1932 (in Chinese)
23 Hwang T W, Han S W, Lee T *et al*. *Journal of Materials Research and Technology*[J], 2020, 9(5): 10447
24 Chen R, Wang H M, Li J *et al*. *Surfaces and Interfaces*[J], 2022, 33: 102197
25 Cai Y C, Cui Y, Zhu L S *et al*. *Surface Engineering*[J], 2021, 37(12): 1496
26 Cai Z B, Cui X F, Liu Z *et al*. *Optics & Laser Technology*[J], 2018, 99: 276
27 Chen S, Richter B, Morrow J D *et al*. *Journal of Manufacturing Processes*[J], 2018, 32: 606
28 Xu J L, Zou P, Liu L *et al*. *Surface and Coatings Technology*[J], 2022, 443: 128615
29 Iams A D, Keist J S, Palmer T A. *Metallurgical and Materials Transactions A*[J], 2020, 51: 982
30 del Abra-Arzola J L, García-Rentería M A, Cruz-Hernández V L *et al*. *Wear*[J], 2018, 400: 43
31 Das B, Gopinath M, Nath A K *et al*. *Journal of the European Ceramic Society*[J], 2018, 38(11): 3932
32 Shang Z X, Shen Y Z, Ji B *et al*. *Metals and Materials International*[J], 2016, 22: 171
33 Eghlimi A, Shamanian M, Eskandarian M *et al*. *Surface and Coatings Technology*[J], 2015, 264: 150
34 Huang F F, Liu E, Qin Y *et al*. *Coatings*[J], 2022, 12(2): 229
35 Erdoğan A. *Proceedings of the Institution of Mechanical Engineers, Part C: Journal of Mechanical Engineering Science*[J], 2022, 236(12): 6873
36 Das T, Erdogan A, Kursuncu B *et al*. *Surface and Coatings Technology*[J], 2020, 403: 126383.
37 Nguyen Q B, Sim Y H M, Gupta M *et al*. *Tribology International*[J], 2015, 82: 464

激光重熔实现水下局部干法激光熔覆双相不锈钢耐磨性能提升

李丛伟[1,2]，朱加雷[2]，曾才有[2]，邓彩艳[1]，从保强[3]，崔　雷[1]，焦向东[2]
(1. 天津大学 材料科学与工程学院，天津 300354)
(2. 北京石油化工学院 机械工程学院，北京 102617)
(3. 北京航空航天大学 机械工程及自动化学院，北京 102206)

摘　要：水下局部干法激光熔覆（ULDLC）是核电站设备原位修复的关键技术。本研究提出采用水下激光重熔技术进一步提升ULDLC制备的双相不锈钢（DSS）涂层的耐磨性能。研究了激光重熔热输入对ULDLC-DSS涂层微观组织及耐磨性能的影响规律。结果表明：DSS涂层初始组织包含魏氏体奥氏体（WA）、晶内奥氏体（IGA）、晶界奥氏体、二次奥氏体（γ_2）及铁素体。随重熔热输入增加，IGA与WA的含量逐渐降低，WA完全消失，铁素体含量显著增加，γ_2相完全溶解，铁素体形貌由片状转变为等轴晶。在最优工艺参数（激光功率3 kW、光斑直径6 mm、扫描速度10 mm/s）下，重熔区显微硬度提升至318.7 HV，增幅达25.7 HV，摩擦系数降低32%，磨损量减少55%。熔覆金属耐磨性能的提升得益于激光重熔导致表面氧化层形成和铁素体晶粒细化的协同作用。

关键词：核电装备；水下激光熔覆；激光重熔；双相不锈钢；耐磨性能

作者简介：李丛伟，男，1997年生，博士，天津大学材料科学与工程学院，天津 300354，E-mail：1022208075@tju.edu.cn